FeS phase diagram and thermal Equation of State under high pressure

Guillaume Morard,[1,2,*] Daniele Antonangeli,[2] Francesca Miozzi,[2,†] Marzena Anna Baron,[2,‡] Eric Edmund,[3] Valerio Cerantola,[4] and Mohamed Mezouar[5]

[1]*Université Grenoble Alpes, Université Savoie Mont Blanc, CNRS, IRD, Université Gustave Eiffel, ISTerre, Grenoble 38000, France*

[2]*Sorbonne Université, Muséum National d'Histoire Naturelle, UMR CNRS 7590, Institut de Minéralogie, de Physique des Matériaux et de Cosmochimie, IMPMC, Paris 75005, France*

[3]*Institüt für Mineralogie, Universität-Münster, Münster 48149, Germany*

[4]*Department of Earth and Environmental Sciences DISAT, University of Milano-Bicocca, Milano I-20126, Italy*

[5]*European Synchrotron Radiation Facility, Boîte Postale 220, Grenoble 38043, France*

(Received 7 January 2025; revised 14 April 2026; accepted 12 May 2026; published 25 June 2026)

FeS is a key end-member iron alloy relevant to the cores of telluric planets. Here, we present a comprehensive study of the FeS phase diagram up to 150 GPa and 3000 K, using *in situ* x-ray diffraction measurements in laser-heated diamond anvil cells. Our results extend the determination of the FeS melting curve up to 100 GPa. We have investigated the subsolidus phase relations of FeS, observing transitions between FeS-VI (MnP-type structure) and FeS-IV (distorded NiAs-type structure). We find that this transition is second-order, with the stability range of FeS-IV narrowing with increasing pressure. Additionally, we identify a novel phase, designated FeS-IX, which is formed at high temperatures above the stability field of FeS-IV, and persists up to the melting point of the alloy. By integrating our data with ambient-temperature literature results, we establish a thermal equation of state for FeS over the investigated pressure and temperature range. These findings carry significant implications for understanding the thermal state and structure of planetary cores, with specific relevance to those of Mercury and Mars.

DOI: 10.1103/h4pj-rvxx

I. INTRODUCTION

Sulfur stands out as an abundant light element alloyed with iron over extended pressure, temperature, and redox conditions, so that the Fe-FeS binary is often used as the reference system to model the properties of the core of telluric planetary bodies. Fe-S compounds are commonly observed in iron meteorites [1], and interpreted as remnants of the cores of small differentiated planetesimals [2]. Sulfur is widely regarded as the primary light element within the core of telluric bodies and planets of varying sizes, ranging from the Moon [3–5] to Mercury [6–8] and Mars [9,10]. Concerning the Earth, the amount of sulphur within its core is still a matter of active debate, with some studies limiting S on the base of its volatility [11], while other arguing for its presence in greater quantity [12]. Irrespective of the geochemical arguments, the physical properties of the Earth's liquid outer core, constrained on the basis of seismological investigations, indicate that sulfur may still contribute significantly to its composition [13–15].

Understanding the thermodynamic properties across the entire binary Fe-S system in an extended pressure range, going from few GPa to hundreds of GPa is thus crucial for advancing our comprehension of planetary cores. Establishing comprehensive thermodynamic models requires knowledge of the phase transitions, melting relations, and equation of state of end-member phases [6,16] which in turn implies investigating the phase diagram and thermo-elastic properties of both Fe and FeS.

FeS has also been extensively studied within the field of condensed matter physics due to its antiferromagnetic semiconducting behavior. Its magnetic and electronic properties vary significantly with both temperature [17] and pressure [18–20]. Given the strong coupling between structure and electronic properties, accurately characterizing its crystallographic structure and the pressure- and temperature-induced phase transition is essential to establish the physical properties of FeS at extreme conditions.

Previous studies on FeS revealed a complex phase diagram, with multiple pressure- and temperature-induced phase transitions [21–29]. However, there is little structural data available close to the melting temperature of FeS, and the stability of many phases have only been constrained after quenching the sample from high temperatures. Notably, diverse structural transformations have been reported in FeS under high pressure, including transitions between NiAs-type and MnP-type structures, a phenomenon frequently observed in transition metal compounds [30–32]. These structural changes may be linked to orbital ordering phenomena, suggesting the existence of an order parameter accounting for the FeS phase diagram under extreme conditions. However, the absence

*Contact author: guillaume.morard@cnrs.fr

†Present address: Department of Earth and Planetary Sciences, ETH Zürich, Zürich, Switzerland and Department of Earth and Environmental Sciences, University of Pavia, Pavia, Italy.

‡Present address: Sorbonne Université, Laboratoire de Chimie de la Matière Condensée de Paris, Paris, France.

 ©2026 American Physical Society

of systematic investigations of the structural evolution of FeS at high pressures and high temperatures hamper our understanding of this ordering phenomena and additionally limit the P-T range covered by equations of state.

In this study, we have determined the phase diagram of FeS up to 150 GPa and 3000 K by *in situ* x-ray diffraction measurements, constraining phase boundaries and identifying a novel phase which is stabilized by high temperatures, close to the melting point of FeS. All the observed phase transitions are of second-order, without a discontinuity in volume. Finally, by integrating our new data with literature results, we have developed a comprehensive thermal equation of state model describing the volume of FeS as a function of pressure and temperature between 40 and 150 GPa and at temperatures up to melting.

II. METHODS

FeS powder from Alfa Aesar (99.9% purity) was used as the starting material for our experiments. All tested commercial powders show evidence of minor extra peaks, indexed as FeS_2 pyrite. This marginal variation from nominal FeS stoichiometry does not influence the results of the present study. FeS powder was compacted into 5–10 μm thick flakes for high-pressure experiments, by compression between two diamonds. Disks of KCl of 15–20 μm thickness were prepared by compressing powder between two carbide anvils and then cut using a femtosecond laser to the desired diameter. KCl disks are used to sandwich the FeS sample, serving as the pressure transmitting medium, as well as providing chemical and thermal insulation from the diamond anvils. KCl also served as the pressure calibrant, following protocols presented in [33] for KCl temperature determination, and using the thermal equation of state in [34]. KCl disks were dried and stored in a vacuum oven to minimize moisture contamination. KCl and the sample were placed into a hole drilled into a pre-indented Re gasket, then compressed between two diamonds in a diamond anvil cell (DAC). Each DAC was left open in the vacuum oven for at least 12 hours after loading to dry the assembly before sealing and pressurizing the sample chamber.

High-pressure experiments were conducted using Le Toullec-type membrane-driven diamond anvil cells. The diamond anvils, with a Boehler-Almax design [35], had culet sizes ranging from 250 to 100/300 beveled tips depending on target pressures. Angle-dispersive x-ray diffraction measurements were carried out at the High-Pressure beamline ID27 at the European Synchrotron Radiation Facility (ESRF) [36]. The x-ray beam was monochromatized at the iodine K-edge (33.6 keV; 0.3738 Å) and focused by KB mirrors to 3×3 μm². Diffraction patterns were recorded using a MARCCD detector. Typical exposure times were five seconds per diffraction pattern. Two fiber lasers were employed to heat the sample from both sides, with focal spots about ∼20 μm in diameter. The area heated by the laser is significantly larger than the dimensions of the x-ray beam to reduce temperature gradients sampled by the x-ray beam. The power of the two lasers were controlled independently, to minimize the difference between the temperature measured on both side of the samples. Spectroradiometric measurements from the upstream side of the DAC allowed us to measure the sample temperature simultaneously with the x-ray diffraction measurements [37]. Temperature uncertainty was estimated to be ±150 K, considering temperature gradients and accuracy in the gray body approximation.

Sample's pressure at high temperature was determined using the known thermal equation of state (EoS) of KCl [34], following the method described in [38]. The temperature of KCl is assumed to be an average between that of the cold portion in contact with the diamond and the temperature measured at the surface of the FeS sample [33]. The accuracy of this method relies on the relatively small thermal expansion of KCl under high pressure, leading to uncertainties in pressure which are less than 5 GPa at the conditions investigated [38].

Diffraction patterns obtained from the experiments were analyzed using the General Structure Analysis System (GSAS) software [39]. Diffraction patterns were fitted using a LeBail method, in order to extract the cell parameters of FeS phases, as well as KCl and FeS_2. Example of an analyzed diffractogram is presented in Fig. S1 of the Supplemental Material (SM) [40]. Cell parameters obtained using the FeS-VI MnP-type orthorhombic structure are presented in Table S1 of the SM [40]. A series of diffraction patterns collected as a function of temperature were analyzed using Rietveld refinement in order to extract the atomic position of Fe and S atoms (Table S2 of the SM [40]). The determined volumes were used to determine the parameters of the thermal equation of state using the EOSFIT package [41]. This software facilitated fitting the experimental data to various equation of state models, enabling the characterization of both the compressibility and thermal behavior of FeS under high-pressure and high-temperature conditions.

Determination of the melting temperature of FeS was conducted following the protocol already successfully employed in the case of FeO by [42]. The onset of melting was identified by the appearance of liquid diffuse scattering at high temperatures, which indicates the loss of long-range order in the sample.

III. RESULTS

A. FeS melting curve

The melting curve of FeS has been determined between 40 and 100 GPa. The temperature where liquid diffuse scattering is first identified in the x-ray diffraction pattern provides an upper bound on the melting temperature, while the temperature associated with the last solid diffraction pattern provides a lower bound; Fig. S2 of the SM [40] shows an example of a heating ramp where melting is observed. This dataset extends the pressure range covered by previous measurements (Williams and Jeanloz, 1990; Boehler, 1992). In particular, the present study agrees with the extrapolation based on the data from Boehler and co-authors. Extrapolations based on earlier data from (Williams and Jeanloz, 1990) would support a melting temperature exceeding 3000 K at 40 GPa, which is 400 K higher than what is reported in the present study.

We fit a melting curve by combining lower pressure results from Boehler (1992) with the present results. Fits to the Simon-Glatzel equation [45] yield the following parameters: $T_0 = 1468$ K, $a = 4.14(1.99)$, and $c = 5.53(0.71)$ (Fig. 1).

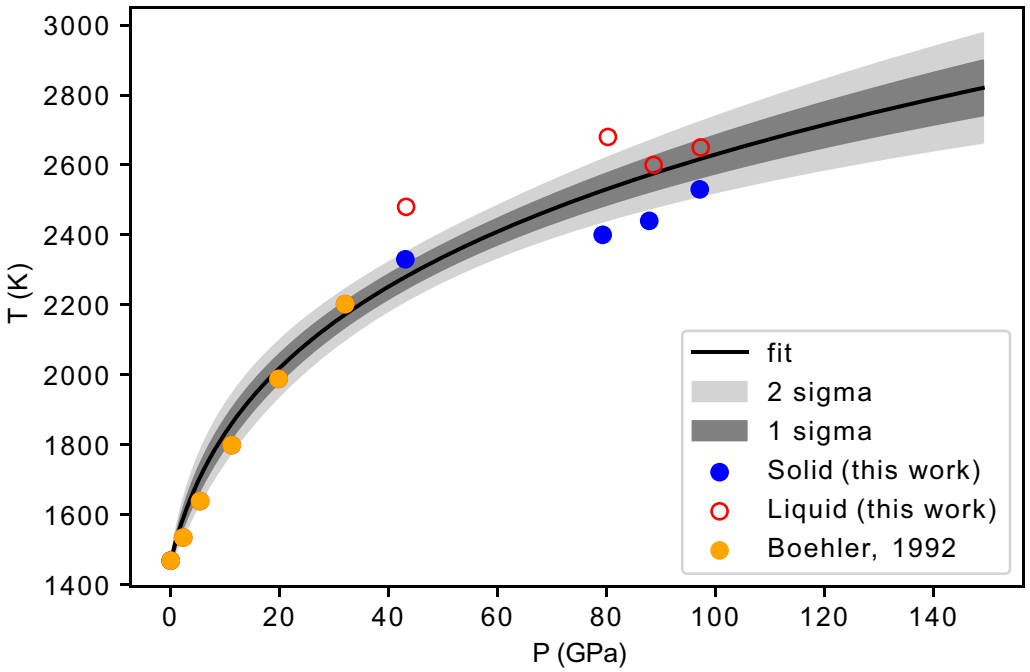


FIG. 1. Melting curve of FeS. Melting points at pressure below 40 GPa have been extracted from [43]. Above 40 GPa (our data), the appearance of diffuse scattering is used to bracket the melting temperature (Table S3 and Fig. S2 of the SM [40]). The Simon-Glatzel fit to the combined dataset is shown by a black line, while confidence intervals at the 1 and 2 sigma level, determined following a Monte Carlo method, are indicated by gray shaded envelopes.

The different P-T conditions used to bracket the melting temperature are listed in Table S3 of the SM [40].

The Simon-Glatzel equation has been widely used over the past decades to interpolate—and occasionally extrapolate—melting curves at high pressures. However, as emphasized by Kennedy and Vaidya [46], its strict validity appears to be largely limited to van der Waals solids, making it potentially inappropriate for extrapolations of melting curves of metals or silicates of geophysical interest. Therefore, we restrict its application to the pressure range investigated in this study. Further experimental data will be needed to accurately constrain the melting temperature of FeS at higher pressures.

B. Second order phase transitions in FeS

The phase diagram of FeS at pressure below 40 GPa is rather well established. Upon compression at ambient temperature FeS-I (troilite) first transforms to FeS-II (MnP-type) and then to FeS-III (monoclinic) [23,47]. With increasing temperature all these phases transform into FeS-IV (hexagonal) [28] and, before melting, into FeS-V (NiAs-type). In particular, the high-temperature phase transition between FeS-IV and FeS-V has been well documented [23,24], as potentially important for understanding the interior of Mars upon cooling. At higher pressures, FeS-III undergoes a transition towards a new FeS-VI structure, discovered at pressures above 30 GPa [26,27]. This phase exhibits an orthorhombic structure, described as a nonmagnetic MnP-type structure [22]. However, the P-T domain of stability for this phase has never been constrained. Discussions on the sequence of low-temperature phases have highlighted changes in symmetry with increasing pressure. Experiments at higher pressure are largely limited to ambient temperature and show a structural transition to the B2 phase (FeS-VII) above 180 GPa [25].

The polymorphism of FeS phases is closely related to the fundamental NiAs structure (a_f and c_f). As detailed in (Kusaba *et al.*, 1998; Terranova and de Leeuw, 2017), relations between hexagonal FeS-IV (P63mc) and NiAs-type (B8) FeS-V (P63/mmc) structures are such that FeS-IV is a super structure of FeS-V ($a = 2a_f$ and $c = c_f$ for FeS-IV, and $a = a_f$ and $c = c_f$ for FeS-V). The anisotropic compressibility of these phases are generally described by the evolution of the c_f/a_f ratio with temperature and pressure [21,48]. FeS-VI is structurally different from FeS-IV and FeS-V, adopting an orthorhombic MnP structure (Pnma). The MnP-type (FeS-VI) structure can also be viewed as a distorted form of the NiAs-related (FeS-IV) structure. When the orthorhombic lattice parameters satisfy the metric relation a is equal to $c/\sqrt{3}$ ($a = c_f/\sqrt{3}$; $b = 2a_f$; $c = c_f$), the distortion vanishes and the two structures become geometrically equivalent. At temperatures close to melting, we were able to identify a new stable structure stable, here designated FeS-IX. This numbering was chosen to avoid confusion, as other numbers have already been assigned to different structures [29]. The FeS-IX structure is also compatible with a MnP type structure, but the cell parameter b is larger than $c/\sqrt{3}$, whereas b is smaller than $c/\sqrt{3}$ in the case of the other MnP structure, FeS-VI.

All diffraction patterns collected between 40 and 150 GPa were fitted with an orthorhombic Pnma structure, which accounts for the observed structural sequence FeS-VI→FeS-IV→FeS-IX. The structural evolution of FeS during a heating cycle at ∼63 GPa is shown in Fig. 2, which includes an enlarged view of the region around $2\theta = 14°$ to better illustrate the transitions.

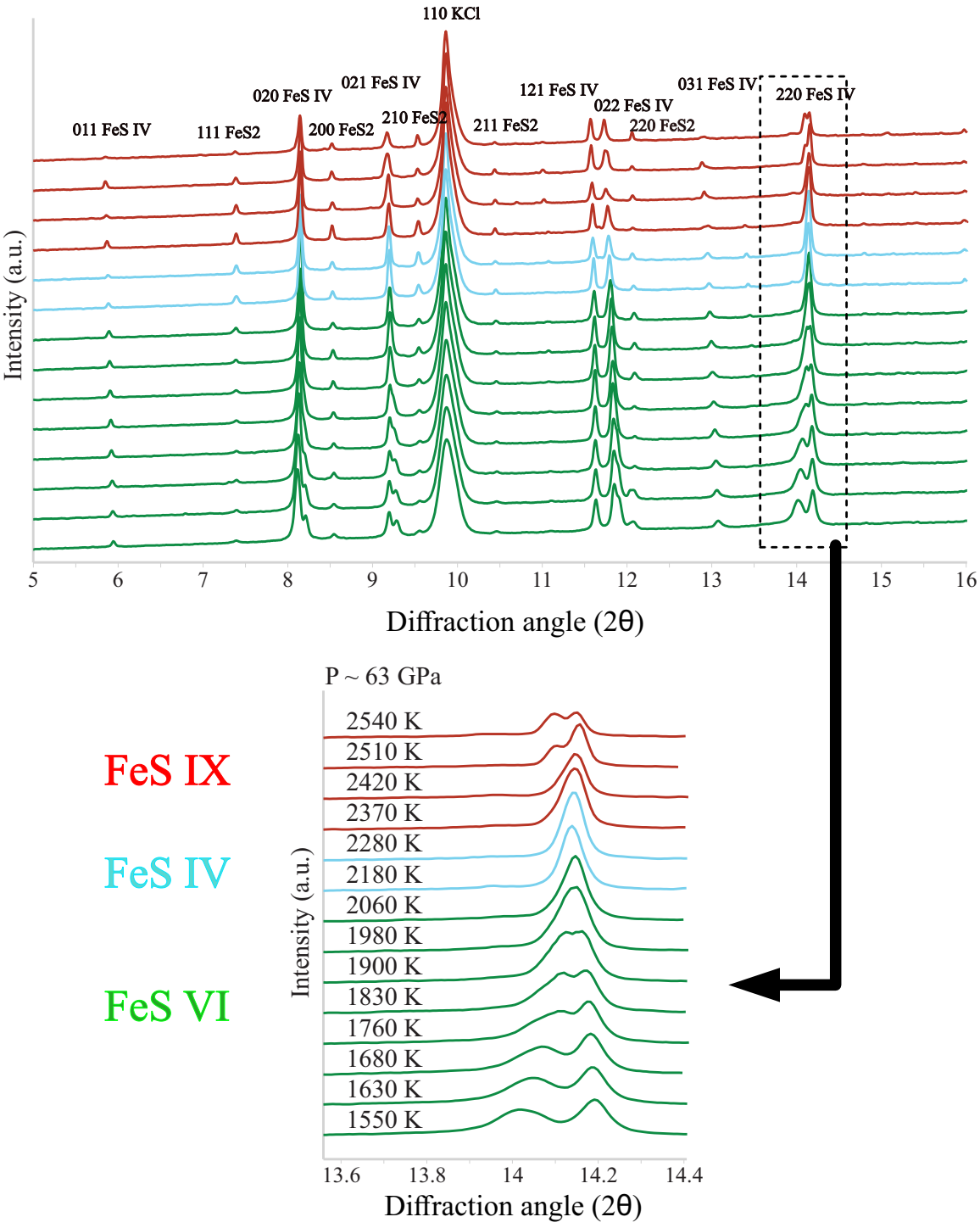


FIG. 2. Temperature-induced phase transition in FeS. Top: Series of diffraction patterns collected for increasing temperature at a starting pressure around 63 GPa (vertically offset for clarity). Diffraction of FeS_2, KCl B2, and FeS-IV are marked. Bottom: Expanded view of the 2θ range corresponding to the 220 peak of FeS-IV, highlighting the peak crossing due to the structural distortion across the phase transition sequence from FeS-VI to FeS-IV and FeS-IX.

The continuous transition shown in Fig. 2 is not accompanied by a volume discontinuity, and can be described as a second order phase transition (Fig. S3 of the SM [40]). This continuous transition can be characterized using an order parameter C, defined as b/(c/$\sqrt{3}$) (Table S1 of the SM [40]). Tracking this ratio for the Pnma MnP structure enabled us to better constrain the stability domain of the different phases: FeS-VI, FeS-IV or FeS-IX (Fig. 3, as well as Fig. S4 of the SM [40]).

Complementary to the Le Bail analysis, Rietveld refinement was applied to a series of diffraction patterns collected during a heating run at increasing temperatures. This enabled us to track the evolution of the Fe and S atomic coordinates as a function of temperature, consistent with the

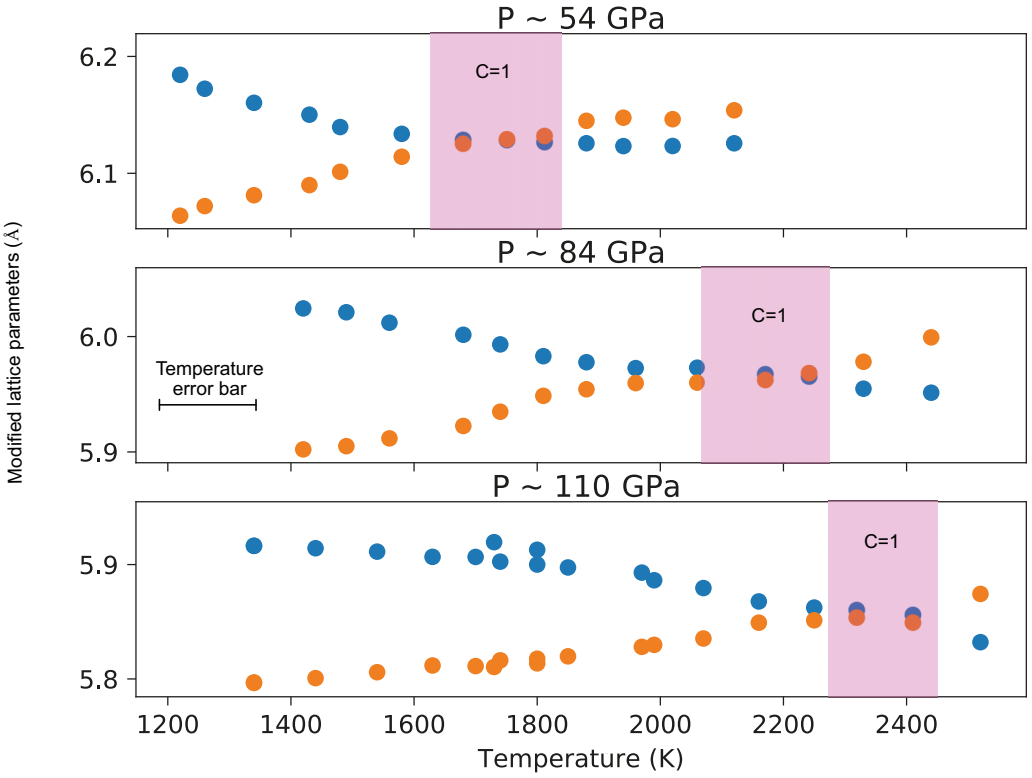


FIG. 3. Temperature evolution of lattice parameters at selected pressures. Blue dots: lattice parameter b multiplied by 2; orange dots: lattice parameter c multiplied by $2/\sqrt{3}$. The lattice parameters are defined by an orthorombic Pnma unit cell. When the two modified lattice parameters are equal, the order parameter C is equal to 1, and the structure is compatible with the hexagonal structure of the FeS-IV phase. C varies from values below 1 (FeS-VI), to values greater than 1 (FeS-IX), and provides a criterion to evaluate the transition sequence across FeS-VI, FeS-IV and FeS-IX. Absolute temperature uncertainties (±150 K) are shown as horizontal bar. Error on the lattice parameters are smaller than the symbols.

second-order phase transitions previously identified from the cell parameter analysis. The results for the x and z coordinates of both atoms are presented in Fig. 4 (the y coordinate is fixed to 0.25).

Similarly to the evolution of the c/a ratio, the x coordinate of the FeS-VI MnP-type structure follows a two-step trend: a rapid change between 1200 and 1500 K, followed by a slight decrease between 1500 and 1650 K toward the more symmetric NiAs-type FeS-IV structure, which remains stable over a ∼200 K interval (1650–1850 K). Above 1850 K, a drastic change occurs, marking the onset of the FeS-IX structure. For the z coordinate, both S and Fe atoms exhibit similar trends: a continuous decrease, a plateau, and then an increase across the three described phases.

Overall, the FeS-VI to FeS-IV transition proceeds in two steps and exhibits characteristics of a continuous transition,

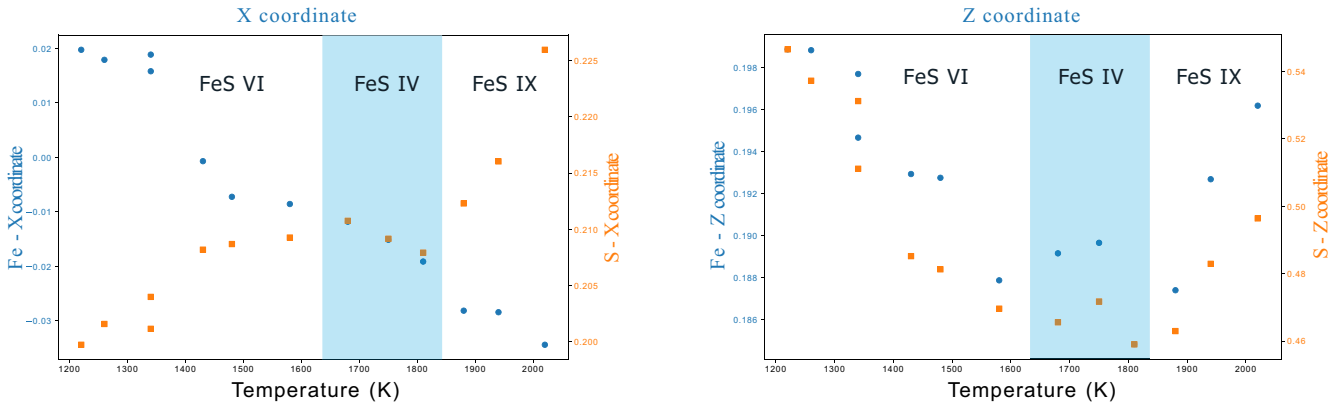


FIG. 4. Evolution of the x and z coordinates of S and Fe atoms as a function of increasing temperature at a pressure of ∼54 GPa (Table S2 of the SM [40]). The y coordinate is fixed at 0.25, in accordance to the Wyckoff positions. Atomic positions were determined by Rietveld refinement of the diffraction patterns.

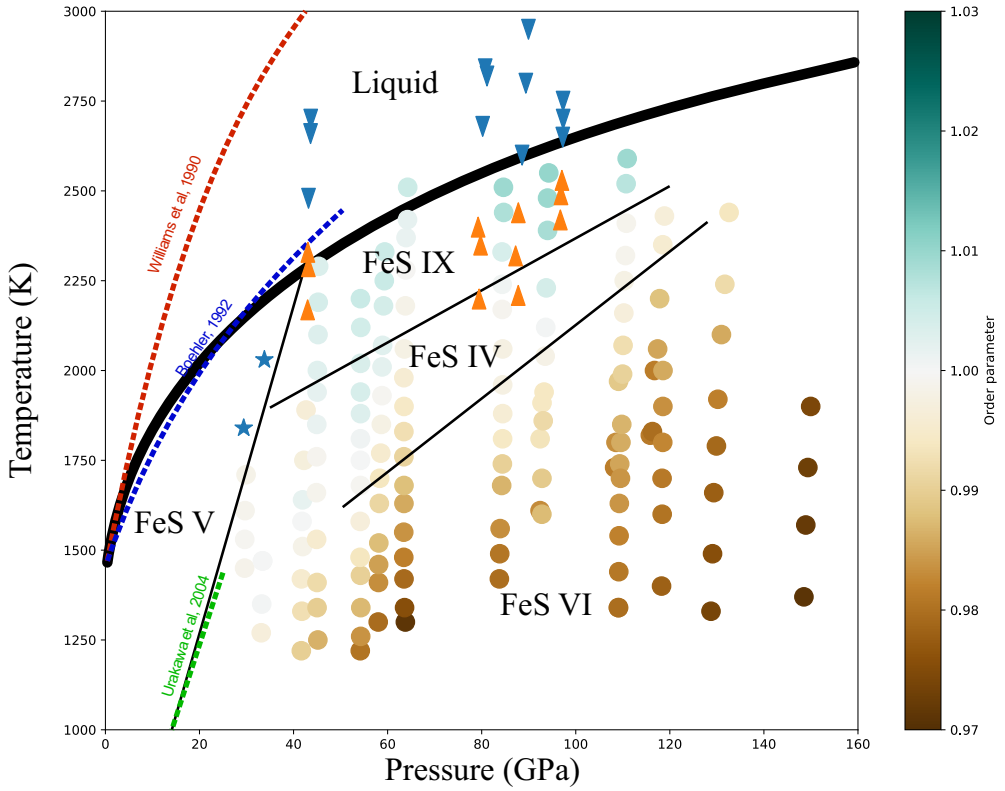


FIG. 5. FeS phase diagram. The different solid phases are highlighted using the parameter C, defined as b/(c/$\sqrt{3}$), which is indicated on a color scale (solid circles). As well, the data points used to define the melting curve illustrated in Fig. 1 are shown as upward (solid) and downward (liquid) triangles. Determined phase boundaries are indicated as black lines. For comparison, the melting curves from [43,44] are also indicated, as well as the FeS-IV to FeS-V boundary from [28].

whereas the FeS-IV to FeS-IX transition is markedly more abrupt. Continuous temperature-induced phase transitions between MnP-type and NiAs-type structures have been documented for various compounds [30] and discussed in relation to their electronic properties [32].

C. FeS phase diagram

The dataset detailing the relationships between various solid phases is presented in Table S1. This dataset encompasses a pressure range from 20 to 150 GPa and temperatures from 1250 K to 2500 K. Figure 4 shows the subsolidus phase diagram and melting line for FeS. Due to the detection limit for temperature measurements by spectroradiometry, the lowest measurable temperature is approximately 1200 K. Consequently, we are unable to constrain the transition between the low-temperature monoclinic phase FeS-III and the higher temperature phases, FeS-IV (at lower pressures) or FeS-VI (at higher pressures).

Our low-pressure experimental results align well with previous studies. In particular, the FeS-V phase boundary (stars in Fig. 5) is consistent with extrapolations of phase lines establish with data reported by Urakawa *et al.* (2004) from multianvil experiments.

At higher pressures, we used the C order parameter as the structural indication of phase transitions. Despite some scattering due to the subtle nature of the transition, two distinct transition lines can be identified (Fig. 5). With increasing temperature FeS-VI transforms into FeS-IV first and to the newly discovered FeS-IX before melting. Extrapolating the established phase boundaries suggests that FeS-VI should be the stable phase at melting only at pressures exceeding 160 GPa. Below this pressure, FeS-IX is the liquidus phase. The triple point IX-V-liquid is located at 42 GPa and 2300 K. The triple point V-IV-IX is estimated at ∼35 GPa and ∼1900 K.

D. Thermal equation of state of FeS phases under high pressure

Along with the phase diagram and transition mechanism, our P-V-T data were used to determine the thermal EoS for FeS. As the observed phase transitions are of second order, we decided to construct a P-V-T relation able to account for the volume as a function of pressure and temperature over the entire explored range, over the stability field of the three phases (FeS-VI, FeS-IV, FeS-IX).

The cold compression curve has been fitted using literature data from [25,26]. Fit to a 3rd order Birch-Murnaghan (BM) formalism yields to the following parameters: $K_0 = 115.5(\pm 27.91)$ GPa; $K' = 4.99(\pm 0.51)$; $V_0 = 15.40(\pm 0.45)\text{cm}^3/\text{mol}$. These results cannot be readily compared with results from previous studies as (Ohfuji *et al.*, 2007) used a modified 3rd order BM formalism, while Ono and Kikegawa (2006) used a 2nd order BM formalism.

The thermal component of the EoS is fit using the Mie-Grüneisen-Debye formalism. To facilitate fitting, using an approach similar to [49], we fixed the Debye temperature that

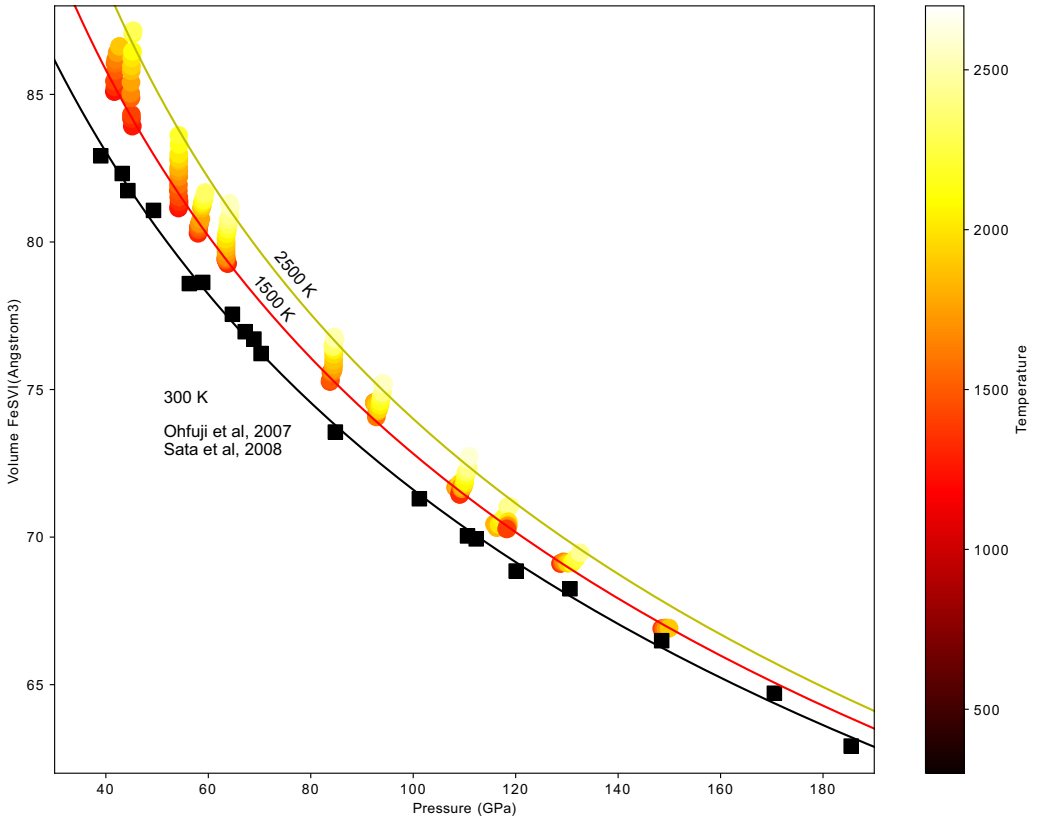


FIG. 6. Thermal EoS for high-pressure FeS phases. Volumes data at 300 K are from literature [25,26]. Three isotherms are indicated: 300, 1500, and 2500 K.

of hcp Fe ($\theta_D = 417$ K [50]), and assumed q = 1. Therefore, only the Grüneisen parameter $\gamma 0$ is refined. The best value obtained is $\gamma 0 = 2.42$ (± 0.03), leading to the thermal EoS fits shown as solid lines in Fig. 6. The quality of the fit can be evaluated by considering the difference between calculated and observed pressure for each datapoint, which never exceeds ± 3 GPa (Fig. S5 of the SM [40]).

IV. DISCUSSION

The present dataset provides a new and clear example of continuous temperature-induced phase transitions between MnP and NiAs structures transitions occurring at high pressure [30]. FeP is observed to adopt the MnP structure found for FeS VI at much lower pressures [51], which has been attributed to differences in the electronic properties of FeP and FeS. It is possible that the FeS-VI to FeS-IV structural transition is connected to the magnetic transition occurring in FeS and Fe-S compounds at high pressure [18,22,52]. To better understand the electronic origins of the transitions between MnP and NiAs-type structures, it would be interesting to track electronic properties, and in particular the spin state, for which experimental constraints are currently limited to high-pressure conditions at ambient temperature [18].

Besides the interesting physics controlling phase stability and material properties, the reported phase diagram is also of significant interest in planetary science. It covers the pressure range expected at the center of Mercury (~40 GPa, e.g. [7]) and Mars (~42 GPa, e.g. [9]) up to conditions reaching those of the Earth's core (136–360 GPa), adding to the existing literature on FeS. The stability field of FeS-IX at temperatures below the melting curve observed in this study hint toward its potential role as one of the phases in the solid portion of medium sized, sulphur-rich terrestrial planetary cores, when pressure encompasses the 40–160 GPa range.

The location of the FeS triple point IX-V-liquid at 42 GPa and 2300 K and of the triple point V-IV-IX at about 38 GPa and 1900 K also provides new insight into the structural evolution of planetary cores. The location of these triple points at conditions directly relevant for the core of Mars and Mercury is of interest for studies addressing the inner structure and thermal evolution of these planets, specifically when dealing with the crystallization of the inner core. Upon cooling, FeS would crystallize either as FeS-V or FeS-IX depending on actual pressures, or as a combination of both phases, with FeS-IX stabilizing at greater depths and FeS-V at slightly lower depths. Furthermore, when assuming Earth-like bottom-up crystallization (crystallization of the core initiating at the planet's center and progressing towards shallower depths over time), the crystallizing inner core would undergo solid-solid transitions upon cooling, leading to a structurally stratified core. While a planetary core made of stochiometric FeS remains hypothetical, the phase diagram and thermal equation of state established here provides valuable insight into the Fe-FeS binary, which is often regarded as an archetypical system for planetary modelling.

ACKNOWLEDGMENTS

This project was supported by the European Research Council (ERC) under the European Unions Horizon 2020 research and innovation programme (Grant Agreement no. 724690) and received funding from the French government, managed by the National Research Agency (ANR), under the France 2030 investment plan, reference 'ANR-22-EXOR-0001'. This work has been also supported by the ANR grant MinDIXI (ANR-22-CE49-0006). M.A.B. and F.M. have received funding from the European Research Council (ERC) under the European Union Horizon 2020 Research and Innovation Programme (Grant Agreement No.670787). E.E. acknowledges support from the DFG through SPP2440 DeepDyn (Grant SA2585/13-1). Femtosecond laser micromachining at the Institut de Minéralogie de Physique des Matériaux et de Cosmochimie (IMPMC), Paris, has been developed and realized by the "Cellule Project" with the financial support of ANR 2010-JCJC-604- 01.

DATA AVAILABILITY

The data that support the findings of this article are openly available [53].

[1] J. H. Jones and M. J. Drake, Experimental investigations of trace element fractionation in iron meteorites. II: The influence of sulfur, Geochim. Cosmochim. Acta **47**, 1199 (1983).

[2] N. L. Chabot, Sulfur contents of the parental metallic cores of magmatic iron meteorites, Geochim. Cosmochim. Acta **68**, 3607 (2004).

[3] R. C. Weber, P.-Y. Lin, E. J. Garnero, Q. Williams, and P. Lognonne, Seismic detection of the lunar core, Science **331**, 309 (2011).

[4] Z. Jing, Y. Wang, Y. Kono, T. Yu, T. Sakamaki, C. Park, M. L. Rivers, S. R. Sutton, and G. Shen, Sound velocity of Fe-S liquids at high pressure: Implications for the Moon's molten outer core, Earth Planet. Sci. Lett. **396**, 78 (2014).

[5] D. Antonangeli, G. Morard, N. C. Schmerr, T. Komabayashi, M. Krisch, G. Fiquet, Y. Fei, and H.-K. Mao, Toward a mineral physics reference model for the Moon's core, Proc. Natl. Acad. Sci. USA **112**, 3916 (2015).

[6] A. Rivoldini, T. Van Hoolst, and O. Verhoeven, The interior structure of Mercury and its core sulfur content, Icarus **201**, 12 (2009).

[7] A. Rivoldini and T. Van Hoolst, The interior structure of Mercury constrained by the low-degree gravity field and the rotation of Mercury, Earth Planet. Sci. Lett. **377–378**, 62 (2013).

[8] S. A. Hauck *et al.*, The curious case of Mercury's internal structure, J. Geophys. Res. Planets **118**, 1204 (2013).

[9] S. C. Stähler *et al.*, Seismic detection of the martian core, Science **373**, 443 (2021).

[10] J. C. E. Irving *et al.*, First observations of core-Transiting seismic phases on Mars, Proc. Natl. Acad. Sci. USA **120**, 1 (2023).

[11] G. Dreibus and H. Palme, Cosmochemical constraints on the sulfur content in the Earth's core, Geochim. Cosmochim. Acta **60**, 1125 (1995).

[12] B. Mahan, J. Siebert, E. A. Pringle, and F. Moynier, Elemental partitioning and isotopic fractionation of Zn between metal and silicate and geochemical estimation of the S content of the Earth's core, Geochim. Cosmochim. Acta **196**, 252 (2017).

[13] G. Morard, J. Siebert, D. Andrault, N. Guignot, G. Garbarino, F. Guyot, and D. Antonangeli, The Earth's core composition from high-pressure density measurements of liquid iron alloys, Earth Planet. Sci. Lett. **373**, 169 (2013).

[14] H. Huang, Y. Fei, L. Cai, F. Jing, X. Hu, H. Xie, L. Zhang, and Z. Gong, Evidence for an oxygen-depleted liquid outer core of the Earth, Nature (London) **479**, 513 (2011).

[15] E. Sumigura-Komabayashi, S. Thompson, T. Komabayashi, D. Freitas, M. Robertson, N. Giordano, A. Pakhomova, and H. P. Liermann, Sulfur—bearing hcp iron for earth's inner core, Geophys. Res. Lett. **53**, e2025GL121618 (2026).

[16] T. Komabayashi, Thermodynamics of melting relations in the system Fe-FeO at high pressure: Implications for oxygen in the Earth's core, J. Geophys. Res. Solid Earth **119**, 4164 (2014).

[17] J. L. Horwood, M. G. Townsend, and A. H. Webster, Magnetic susceptibility of single-crystal $Fe_{1-x}S$, J. Solid State Chem. **17**, 35 (1976).

[18] J.-P. Rueff, C. -C. Kao, V. V. Struzhkin, J. Badro, J. Shu, R. J. Hemley, and H. K. Mao, Pressure induced high-spin to low-spin transition in FeS evidenced by x-ray emission spectroscopy, Phys. Rev. Lett. **82**, 3284 (1999).

[19] K. Shimada, T. Mizokawa, K. Mamiya, T. Saitoh, A. Fujimori, K. Ono, A. Kakizaki, and T. Ishii, Spin-integrated and spin-resolved photoemission study of Fe chalcogenides, Phys. Rev. B - Condens. Matter Mater. Phys. **57**, 8845 (1998).

[20] S. Takele and G. R. Hearne, Electrical transport, magnetism, and spin-state configurations of high-pressure phases of FeS, Phys. Rev. B - Condens. Matter Mater. Phys. **60**, 4401 (1999).

[21] K. Kusaba, Y. Syono, T. Kikegawa, and O. Shimomura, High pressure and temperature behavior of FeS, J. Phys. Chem. Solids **59**, 945 (1998).

[22] S. Ono, A. R. Oganov, J. P. Brodholt, L. Vočadlo, I. G. Wood, A. Lyakhov, C. W. Glass, A. S. Côté, and G. D. Price, High-pressure phase transformations of FeS: Novel phases at conditions of planetary cores, Earth Planet. Sci. Lett. **272**, 481 (2008).

[23] Y. Fei, C. T. Prewitt, H. Mao, and C. M. BERTKA, Structure and density of FeS at high pressure and high temperature and the internal structure of mars, Science **268**, 1892 (1995).

[24] A. Kavner, T. S. Duffy, and G. Shen, Phase stability and density of FeS at high pressures and temperatures: Implications for the interior structure of Mars, Earth Planet. Sci. Lett. **185**, 25 (2001).

[25] N. Sata, H. Ohfuji, K. Hirose, H. Kobayashi, Y. Ohishi, and N. Hirao, New high-pressure B2 phase of FeS above 180 GPa, Am. Mineral. **93**, 492 (2008).

[26] H. Ohfuji, N. Sata, H. Kobayashi, Y. Ohishi, K. Hirose, and T. Irifune, A new high-pressure and high-temperature polymorph of FeS, Phys. Chem. Miner. **34**, 335 (2007).

[27] S. Ono and T. Kikegawa, High-pressure study of FeS, between 20 and 120 GPa, using synchrotron x-ray powder diffraction, Am. Mineral. **91**, 1941 (2006).

[28] S. Urakawa, K. Someya, H. Terasaki, T. Katsura, S. Yokoshi, K. ichi Funakoshi, W. Utsumi, Y. Katayama, Y. ichiro Sueda, and T. Irifune, Phase relationships and equations of state for FeS at high-pressure temperatures and implications for the internal structure of Mars, Phys. Earth Planet. Inter. **143–144**, 469 (2004).

[29] U. Terranova and N. H. de Leeuw, Phase stability and thermodynamic properties of FeS polymorphs, J. Phys. Chem. Solids **111**, 317 (2017).

[30] K. Selte and A. Kjekshus, On phase transittions betweeen the MnP- and NiAs-type structures, Acta Chem. Scand. **27**, 3195 (1973).

[31] H. F. Franzen, C. Haas, and F. Jellinek, Phase transitions between NiAs- and MnP-type phases, Phys. Rev. B **10**, 1248 (1974).

[32] W. Tremel, R. Hoffmann, and J. Silvestre, Transitions between NiAs- and MnP-Type Phases: An electronically driven distortion of triangular (36) nets, J. Am. Chem. Soc. **108**, 5174 (1986).

[33] A. J. Campbell, L. Danielson, K. Righter, C. T. Seagle, Y. Wang, and V. B. Prakapenka, High-pressure effects on the iron-iron oxide and nickel-nickel oxide oxygen fugacity buffers, Earth Planet. Sci. Lett. **286**, 556 (2009).

[34] A. Dewaele, A. B. Belonoshko, G. Garbarino, F. Occelli, P. Bouvier, M. Hanfland, and M. Mezouar, High-pressure-high-temperature equation of state of KCl and KBr, Phys. Rev. B - Condens. Matter Mater. Phys. **85**, 1 (2012).

[35] R. Boehler and K. De Hantsetters, New anvil designs in diamond-cells, High Press. Res. **24**, 391 (2004).

[36] M. Mezouar *et al.*, Development of a new state-of-the-art beamline optimized for monochromatic single-crystal and powder x-ray diffraction under extreme conditions at the ESRF, J. Synchrotron Radiat. **12**, 659 (2005).

[37] M. Mezouar *et al.*, Methodology for *in situ* synchrotron x-ray studies in the laser-heated diamond anvil cell, High Press. Res. **37**, 170 (2017).

[38] F. Miozzi, G. Morard, D. Antonangeli, A. N. Clark, M. Mezouar, C. Dorn, A. Rozel, and G. Fiquet, Equation of state of SiC at extreme conditions: New insight into the interior of carbon-rich exoplanets, J. Geophys. Res. E Planets **123**, 1 (2018).

[39] B. H. Toby, EXPGUI, a graphical user interface for GSAS, J. Appl. Cryst. **34**, 210 (2001).

[40] See Supplemental Material at http://link.aps.org/supplemental/10.1103/h4pj-rvxx for additional information on the data analysis.

[41] J. Gonzalez-Platas, M. Alvaro, F. Nestola, and R. Angel, EosFit7-GUI: A new graphical user interface for equation of state calculations, analyses, and teaching, J. Appl. Crystallogr. **49**, 1377 (2016).

[42] G. Morard, D. Antonangeli, J. Bouchet, A. Rivoldini, S. Boccato, F. Miozzi, E. Boulard, and H. Bureau, Structural and electronic transitions in liquid FeO under high-pressure journal of geophysical research: Solid earth, J. Geophys. Res., Solid Earth **127**, e2022JB025117 (2022).

[43] R. Boehler, Melting of the Fe–FeO and the Fe–FeS systems at high pressure: Constraints on core temperatures, Earth Planet. Sci. Lett. **111**, 217 (1992).

[44] Q. Williams and R. Jeanloz, Melting relations in the iron-sulfur system at ultra-high pressures: Implications for the thermal state of the earth, J. Geophys. Res. **95**, 19299 (1990).

[45] F. Simon and G. Glatzel, Bernerkungen zur schmelzdruckkurve, Z. Anorg. Allg. Chem. **178**, 309 (1929).

[46] G. C. Kennedy and S. N. Vaidya, The effect of pressure on the melting temperature of solids, J. Geophys. Res. **75**, 1019 (1970).

[47] W. Marshall, R. Nelmes, J. Loveday, S. Klotz, J. Besson, G. Hamel, and J. Parise, High-pressure neutron-diffraction study of FeS, Phys. Rev. B **61**, 11201 (2000).

[48] B. Zhao, G. Morard, S. Boccato, M. Mezouar, and D. Antonangeli, Phase diagram and thermo-elastic properties of Fe-S compounds up to 15 GPa: Thermodynamic constraints on the core of medium-sized telluric planets, Earth Planet. Sci. Lett. **634**, 118676 (2024).

[49] S. Thompson, T. Komabayashi, H. Breton, S. Suehiro, K. Glazyrin, A. Pakhomova, and Y. Ohishi, Compression experiments to 126 GPa and 2500 K and thermal equation of state of Fe_3S: Implications for sulphur in the Earth's core, Earth Planet. Sci. Lett. **534**, 116080 (2020).

[50] A. Dewaele, P. Loubeyre, F. Occelli, M. Mezouar, P. I. Dorogokupets, and M. Torrent, Quasihydrostatic equation of state of Iron above 2 Mbar, Phys. Rev. Lett. **97**, 29 (2006).

[51] T. Gu, X. Wu, S. Qin, and L. Dubrovinsky, *In situ* high-pressure study of FeP: Implications for planetary cores, Phys. Earth Planet. Inter. **184**, 154 (2011).

[52] J. F. Lin, Y. Fei, W. Sturhahn, J. Zhao, H. K. Mao, and R. J. Hemley, Magnetic transition and sound velocities of Fe3S at high pressure: Implications for Earth and planetary cores, Earth Planet. Sci. Lett. **226**, 33 (2004).

[53] G. Morard, FeS XRD Data, (2025), doi: 10.6084/m9.figshare.28143683.